Algorithm Theoretical Basis Document for

MTG Land SAF Surface Temperature (MTLST)

PRODUCTS: LSA-007 (MTLST)

Reference Number:	SAF/LAND/IPMA/ATBD_MTLST/1.0
Issue/Revision Index:	Issue 1
Last Change:	05/01/2017

DOCUMENT SIGNATURE TABLE

	Name	Date	Signature
Prepared by :	J. Martins, I. Trigo.		
Approved by :	Land SAF Project Manager (IPMA)		

DOCUMENTATION CHANGE RECORD

Issue / Revision	Date	Description:
Version 1.0	05/01/2017	MTLST algorithm for the FCI on MTG

DISTRIBUTION LIST

Internal Consortium Distribution		
Organisation	**Name**	**No. Copies**
IPMA	Isabel Trigo	
IPMA	Sandra Coelho e Freitas	
IPMA	Carla Barroso	
IPMA	Isabel Monteiro	
IPMA	João Paulo Martins	
IPMA	Pedro Diegues	
IPMA	Ana Veloso	
IPMA	Pedro Ferreira	
IDL	Carlos da Camara	
IDL	Teresa Calado	
KIT	Folke-S. Olesen	
KIT	Frank Goettsche	
MF	Jean-Louis Roujean	
MF	Gregoire Jacob	
MF	Dominique Carrer	
RMI	Françoise Meulenberghs	
RMI	Arboleda Alirio	
RMI	Nicolas Ghilain	
UV	Joaquin Melia	
UV	F. Javier García Haro	
UV/EOLAB	Fernando Camacho	
UV	Aleixander Verger	

External Distribution		
Organisation	**Name**	**No. Copies**
EUMETSAT	Frédéric Gasiglia	
EUMETSAT	Dominique Faucher	
EUMETSAT	Lorenzo Sarlo	
EUMETSAT	Lothar Schueller	
EDISOFT	Tiago Sepúlveda	
EDISOFT	Joana Rosa	
EDISOFT	Joaquim Araújo	
GMV	Mauro Lima	

Steering Group Distribution		
Nominated by:	**Name**	**No. Copies**
IPMA	Pedro Viterbo	
EUMETSAT	Lothar Schueller	
EUMETSAT	Christopher Hanson	
EUMETSAT	Harald Rothfuss	
STG/AFG	Francesco Zauli	
MF	Jean-François Mahfouf	
RMI	Rafiq Hamdi	
KIT	Johannes Orphal	
VITO	Bart Deronde	

Table of Contents

List of Figures

1 Introduction

The EUMETSAT Satellite Application Facility on Land Surface Analysis (Land-SAF) is dedicated to the retrieval of information on land surfaces from remote sensing data, with emphasis on EUMETSAT satellites. The Land-SAF provides near-real-time and offline products and user support for a wide range of land surface variables related with: (i) surface radiation, both long- and short-wave components; (ii) vegetation, including state, stress and wild fires; and (ii) the energy budget at the surface, combining information on the radiation budget and vegetation state. The document presents the algorithm used by the Land-SAF for the estimation of *Land Surface Temperature* (LST), Land-SAF product LSA-007, from the upcoming sensor Flexible Combined Imager (FCI) on-board Meteosat Third Generation (MTG).

LST is an important parameter for the monitoring of surface energy budget, since it is the primary variable determining the upward thermal radiation and one of the main controllers of sensible and latent heat fluxes between the surface and the atmosphere. Thus, the reliable and long-term estimation of LST is extremely important for a wide number of applications, including amongst others: (i) model validation (Mitchell *et al.*, 2004; Trigo *et al.*, 2015; Trigo and Viterbo, 2003), (ii) data assimilation (Bosilovich *et al.*, 2007; Caparrini *et al.*, 2004; Qin *et al.*, 2007; Ghent *et al.*, 2010; Bateni *et al.*, 2013); (iii) hydrological applications (Kustas and Norman, 1996; Wan *et al.*, 2004); and (iv) climate monitoring (Jin, 2004; Jin *et al.*, 2005; Yu *et al.*, 2008; Duguay-Tetzlaff *et al.*, 2015).

Land-SAF has been providing LST products based on SEVIRI on-board the MSG series (Schmetz *et al.*, 2002) as well as for the AVHRR on-board the Metop polar orbiting satellites, using a well-established methodology (Freitas *et al.*, 2010; Martins *et al.*, 2016), on which the LSA-007 (MTLST) product will be based. Both MSG and MTG based products use the full spatial and temporal resolution of the sensors, allowing for a complete monitoring of the diurnal cycle over clear-sky regions.

LST estimations from remotely sensed data are generally obtained from one or more channels within the thermal infrared atmospheric window from 8-to-13 µm (Dash *et al.*, 2001; Li *et al.*, 2013). Operational LST retrievals often make use of split-window algorithms (e.g., Prata, 1993; Wan and Dozier, 1996), where LST is obtained through a semi-empirical regression of top-of-atmosphere (TOA) brightness temperatures of two pseudo-contiguous channels, i.e., the split-window channels. The Land-SAF LST algorithm is based on the generalised split-window (GSW) formulation initially developed for AVHRR and MODIS (Wan and Dozier, 1996), now adapted to SEVIRI split-window channels (Freitas *et al.*, 2010). The error of LST retrievals via GSW depends on (i) the uncertainty of surface emissivity, (ii) the water vapour content of the atmosphere, and (iii) or the satellite view angle. Because the latter determines the total optical path, LST estimations are often limited to satellite zenith angles (SZA) below ~60°, where retrieval errors are still acceptable (e.g, Jiménez-Muñoz and Sobrino, 2006; Sun and Pinker, 2003; Wan and Dozier, 1996). In the case of geostationary platforms, already unable to provide the global coverage of polar-orbiters, such view angle restrictions pose additional limitations to the product spatial coverage. A wider retrieval area must be carefully weighed against an increasing error.

Any parameter inference is of little usefulness without an uncertainty measure. Here, we discuss the calibration of the GSW algorithm used operationally by the Land-SAF and the respective assessment of LST retrieval errors. These errors take into account the expected performance of the GSW under different atmospheric conditions, as well as the characterization of input uncertainties and their propagation to the final LST estimation.

2 Flexible Combined Imager (FCI) / Meteosat Third Generation (MTG)

Meteosat Third Generation (MTG) series of satellites is actually a "Twin Satellite Concept", based on 3-axis platforms, composed by four imaging satellites (MTG-I) (20 years of operational services expected) and two sounding satellites (MTG-S) (15.5 years of operational services expected). The imaging satellites, MTG-I, will fly the Flexible Combined Imager (FCI) and the Lightning Imager (LI), an imaging lightning detection instrument. The sounding satellites, MTG-S, will include an interferometer, the Infra-red Sounder (IRS), with hyper-spectral resolution in the thermal spectral domain, and the Sentinel-4 instrument, the high resolution Ultraviolet Visible Near-infrared (UVN) spectrometer. Such improvements are necessary to achieve compliance with more demanding user requirements on spatial resolution; repeat cycle and signal-to -noise ratio, and are a prerequisite to conduct soundings from geostationary orbit.

The Flexible Combined Imager (FCI) on the MTG-I satellite will continue the very successful operation of the SEVIRI on MSG. The satellite's three axes stabilised platform will be capable of providing additional channels with better spatial, temporal and radiometric resolution, compared to the current MSG satellites. Requirements for the FCI have been formulated by regional and global Numerical Weather Prediction (NWP) and Nowcasting communities. These requirements are reflected in the design which allows for Full Disk Scan (FDS), with a basic repeat cycle of 10 minutes, and a European Regional-Rapid-Scan (RRS) which covers one-quarter of the full disk with a repeat cycle of 2.5 minutes. The FCI takes measurements in 16 channels (as detailed in Table 1), of which eight are placed in the solar spectral domain between 0.4 µm to 2.1 µm, delivering data with a 1 km spatial resolution. The additional eight channels are in the thermal spectral domain between 3.8 µm to 13.3 µm, delivering data with a 2 km spatial resolution. In the RRS mode there will be two additional channels in the solar domain, with a spatial resolution of 0.5 km, and two in the thermal domain, with a spatial resolution of 1 km. Further information may be found at EUMETSAT website (http://www.eumetsat.int).

The LSA-007 product is to be generated using FCI measurements in FDS mode only, and following an algorithm similar to that implemented for SEVIRI-based LSA-001 product, where LST is estimated from top-of-atmosphere measurements of brightness temperatures within the split-window spectral region. The FCI will have a slightly different configuration of the available channels when compared to SEVIRI. The LSA-007 LST algorithm will be based on FCI split-window channels (10.5 µm and 12.3 µm), which correspond to the 10.8 µm and 12.0 µm in SEVIRI. The preliminary theoretical response functions of those channels (made available by the Numerical Weather Prediction SAF

here https://nwpsaf.eu/downloads/rtcoef_rttov11/ir_srf/rtcoef_mtg_1_fci_srf.html, Figure 1) shows that in the FCI, the response functions will be narrower.

Channel	Centre Wavelength	Spectral Width	Spatial Sampling Distance (SSD)
VIS 0.4	0.444 µm	0.060 µm	1.0 km
VIS 0.5	0.510 µm	0.040 µm	1.0 km
VIS 0.6	0.640 µm	0.050 µm	1.0 km; 0.5 km*
VIS 0.8	0.865 µm	0.050 µm	1.0 km
VIS 0.9	0.914 µm	0.020 µm	1.0 km
NIR 1.3	1.380 µm	0.030 µm	1.0 km
NIR 1.6	1.610 µm	0.050 µm	1.0 km
NIR 2.2	2.250 µm	0.050 µm	1.0 km; 0.5 km*
IR 3.8 (TIR)	3.800 µm	0.400 µm	2.0 km; 1.0 km*
WV 6.3	6.300 µm	1.000 µm	2.0 km
WV 7.3	7.350 µm	0.500 µm	2.0 km
IR 8.7 (TIR)	8.700 µm	0.400 µm	2.0 km
IR 9.7 (O_3)	9.660 µm	0.300 µm	2.0 km
IR 10.5 (TIR)	10.500 µm	0.700 µm	2.0 km; 1.0 km*
IR 12.3 (TIR)	12.300 µm	0.500 µm	2.0 km
IR 13.3 (CO_2)	13.300 µm	0.600 µm	2.0 km

Table 1 – List of FCI/MTG channels. The channels VIS 0.6, NIR 2.2, IR 3.8 and IR 10.5 are delivered in both FDS and RRS sampling configurations; the latter is indicated by * in the table (data from: http://www.eumetsat.int/website/home/Satellites/FutureSatellites/MeteosatThirdGeneration/MTGDesign/index.html#fci).

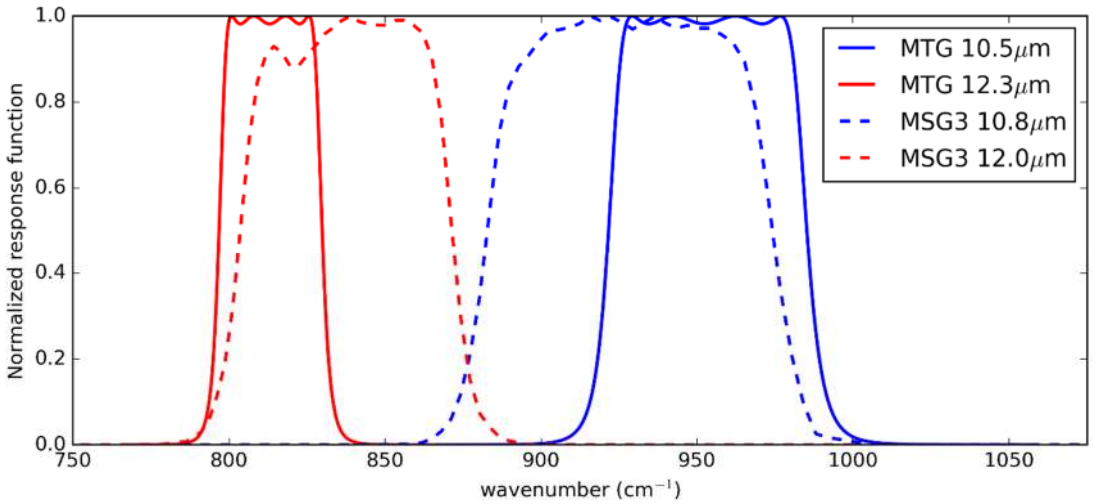

Figure 1 – Preliminary normalized response functions for FCI/MTG split-window channels (provided by the NWP SAF http://nwpsaf.eu/, solid lines). The response functions of SEVIRI corresponding channels are also displayed (SEVIRI/MSG3, dashed lines).

3 The Land-SAF LST Retrieval algorithm

3.1 Generalized Split-Windows

Several algorithms have been proposed to retrieve LST from remotely sensed thermal infrared data (e.g., Coll *et al.*, 2006; Dash *et al.*, 2001; Gao *et al.*, 2013; Jiang and Li, 2008; Jiménez-Muñoz and Sobrino, 2006; Prata, 2002; Sobrino and Romaguera, 2004; Sun and Pinker, 2003; Yu *et al.*, 2008; Li *et al.*, 2013). The current Land-SAF LST products estimated from SEVIRI/MSG and AVHRR/Metop make use of Generalized Split-Window (GSW) algorithms with formulations similar to that first proposed by Wan and Dozier (1996) for AVHRR and MODIS. Thus, LST is as a function of TOA brightness temperatures measured by the two split-window channels IR1 and IR2 (Freitas *et al.*, 2010):

$$LST = C + \left(A_1 + A_2\frac{1-\epsilon}{\epsilon} + A_3\frac{\Delta\epsilon}{\epsilon^2}\right)\frac{T_{IR1}+T_{IR2}}{2} + \left(B_1 + B_2\frac{1-\epsilon}{\epsilon} + B_3\frac{\Delta\epsilon}{\epsilon^2}\right)\frac{T_{IR1}-T_{IR2}}{2} + \Delta LST, \quad (1)$$

where $A_1, A_2, A_3, B_1, B_2, B_3$ and C are the model coefficients, T_{IR1} and T_{IR2} are the top-of-atmosphere equivalent brightness temperatures of the two split-window channels, respectively, $\epsilon = (\epsilon_{IR1} + \epsilon_{IR2})/2$ and $\Delta\epsilon = \epsilon_{IR1} - \epsilon_{IR2}$ are the average and the difference of the emissivities in the split-windows channels and ΔLST is the algorithm uncertainty. The regression coefficients are fit for classes of total column water vapour (TCWV) and satellite zenith angle (ZVA), and they must somehow simulate atmospheric absorption and emission, while the effect of surface emissivity is, in these cases, explicitly resolved. The atmospheric transmissivity is mainly constrained by the radiative optical path. Hence, a good calibration database to fit model coefficients in Equation (1) needs to ensure that a scene may be observed by a wide range of viewing geometries (ZVA) and water vapor contents, which is the most relevant and variable absorber/emitter in the thermal IR window region.

The difference between TOA brightness temperatures in the split-window channels is aimed at capturing differential absorption within those bands which is associated to atmospheric water vapor content. In the case of a GSW algorithm, Equation (1), the difference between the spectral emissivities of the window channels are also taken into account. This difference is related to surface type and moisture in the sense that moister surfaces show less spectral variations in emissivity (Hulley *et al.*, 2015).

3.2 Radiative Transfer Simulations

The development of LST algorithms is usually based on a set of radiative transfer simulations performed for a calibration database (for algorithm fit) and a validation one (for algorithm test), both representing a wide range of clear sky conditions. The databases must be independent and, while the former should encapsulate the widest

possible atmospheric conditions for the area of interest together with broad distributions of surface emissivity and sensor viewing geometry that are needed for robust parameter estimation, the latter should contain the largest possible set of profiles/surface conditions to allow a comprehensive characterization of LST algorithm uncertainty. By LST algorithm uncertainty, we mean deviations of LST retrievals from the "true value" that are not associated to uncertainties in the input data, but solely to the retrieval method. The characterization of the individual sources of uncertainty (such as the algorithm uncertainty or the uncertainty due to emissivity or to the sensor noise, for example) has been recognized as crucial for the uncertainty validation of remotely sensed surface temperature products (Bulgin *et al.*, 2016). It is worth emphasizing that the comparison of LST estimates obtained using actual remote sensing observations against ground-based observations is part of a product validation exercise. In that case, which is often limited to a relatively small number of available sites, the deviations will be the result of both algorithm and input errors and their contributions to the total error are impossible to disentangle. The radiative transfer simulations aim to determine the TOA spectral radiances for each profile in the respective databases, so that the forward problem is solved with full knowledge of the surface emission and atmospheric absorption. It is important that those simulations are performed with an accurate radiative transfer model. The simulations were performed using the MODTRAN4 code (Berk *et al.*, 1999), which returns spectral radiances (L_ν) with a resolution of 1 cm^{-1}. For the sake of simplicity, MODTRAN4 TOA radiances were convoluted with FCI response functions for channels IR 10.5 and IR 12.3 (Figure 1) using their central frequency (Table 1):

$$L_i = \frac{\int_{\nu_{i,1}}^{\nu_{i,2}} \phi_{i,\nu}\, L_\nu d\nu}{\int_{\nu_{i,1}}^{\nu_{i,2}} \phi_{i,\nu} d\nu}, \tag{2}$$

where $\nu_{i,1}$ and $\nu_{i,2}$ are the lower and upper wavenumber boundaries of the channel, respectively; the integrals in (2) are estimated taking into account the full tabulated values of the response function $\phi_{i,\nu}$, i.e., between $\nu_1 = 870\ \mathrm{cm}^{-1}$ and $\nu_2 = 1050\ \mathrm{cm}^{-1}$, for channel IR 10.5, and between $\nu_1 = 770\ \mathrm{cm}^{-1}$ and $\nu_2 = 860\ \mathrm{cm}^{-1}$, for channel IR 12.3. Those values are then subject to the inverse Planck function, B^{-1}, to obtain an estimate of the respective channels brightness temperatures, T^*_{IR1} and T^*_{IR2} (e.g., Freitas *et al.*, 2013):

$$T_i^* = B^{-1}(\nu_{i,c}, L_i) = \frac{c_2 \nu_{i,c}}{\log\left(\frac{c_1 \nu_{i,c}^3}{L_i} + 1\right)}, \tag{3}$$

where $\nu_{i,c}$ is the central frequency of each channel (calculated from the values in Table 1), $c_1 = 1.19104{\times}10^{-5}\mathrm{mW.cm}^2$ and $c_2 = 1.43877\ \mathrm{K.cm}$ are constants. Finally, band-correction coefficients are applied to account for the fact that the central frequency was used instead of the whole range of spectral radiances. The correction adopted here takes the form:

$$T_i = A + BT_i^*, \quad (4)$$

The coefficients were derived calculating a series of L_i values (taking into account the channel response function according to Eq. (2)) for T values in the range $[170,370]$ K and followed by a linear regression between the prescribed T and the calculated $T^* = B^{-1}(\nu_{i,c}, L_i)$. The estimated coefficient values are presented in **Erro! A origem da referência não foi encontrada.**. The whole procedure will be repeated for the response functions to be provided for each FCI of the MTG series.

Channel	ν_c (cm^{-1})	A	B
IR 10.5	926.103	-0.211883	1.00070
IR 12.3	813.387	-0.05792	1.00022

Table 2 - Band-correction coefficients for the split-window channels of the FCI.

3.3 Calibration/Verification Database

The radiative transfer simulations described above are grouped into two independent sets: one is used to calibrate the model (i.e. to determine the values of the coefficients A_i, B_i and C for each class of ZVA and TCWV) and the other is used for an independent validation and to infer the algorithm uncertainty. Both sets use a clear-sky profile database hereafter referred to as SeeBor, which compiles over 15,700 temperature, water vapour and ozone profiles, together with their spectral emissivity, land cover, elevation, skin temperature (here referred as T_{skin}), and surface pressure, put together by Borbas *et al.* (2005). T_{skin} corresponds effectively to land, sea, lake or ice surface temperature, depending on the profile location. These profiles are representative of a wide range of atmospheric conditions over the whole globe. The calibration process needs to be addressed carefully as the algorithm performance is very sensitive to the calibration methodology. Here, the methodology proposed by Martins *et al.* (2016) was followed, although alternative strategies have recently been proposed (Mattar *et al.*, 2015). Given the physical constraints of the problem and the range of the input parameters (Martins *et al.*, 2016), the following methodology is used to select the subset of calibration profiles:

(1) Define classes of $\mathrm{T_{Skin}}$ (from 200 K to 330 K in steps of 5 K) and TCWV (from 0 to 6 cm in classes of 0.75 cm—values greater than this should be treated with the coefficient corresponding to the last TCWV class).

(2) Iterate in the SeeBor clear-sky profile database to fill each class in the $\mathrm{TCWV/\ T_{Skin}}$ "phase space" with one case each. When a new profile is selected, it is ensured that its great-circle distance to the already selected profiles is greater than an initial distance of 15 degrees, which guarantees a wide

geographical coverage. After a sufficiently large number of tries (in this case 30,000), the distance criterion is relaxed in steps of minus 1 degree, until the whole $\mathrm{TCWV}/\ \mathrm{T_{Skin}}$ phase space is filled.

(3) For each of the previously selected profiles, assign a new $\mathrm{T_{Skin}}$ based on the observed ranges of $\mathrm{T_{Skin}} - \mathrm{T_{air}}$, where $\mathrm{T_{air}}$ is the near surface air temperature. The choice of the range of perturbations to apply is key to the performance of the chosen model and may depend on the region of interest. In the case of the Meteosat disk, a range of ±15 K around $\mathrm{T_{air}}$ in steps of 5 K showed an overall good performance.

(4) Each of these conditions may be sensed from angles ranging from 0 (nadir view) to 70° in steps of 2.5°, starting in 1.25°. This way, each ZVA class will be populated with two equally spaced angles. It is important to discretize the viewing geometry in this way because this is an intrinsically non-linear problem. The upper limit of the ZVA might be adapted for the sensor under analysis. Previous calibration exercises show that above this viewing angle limit the retrieval errors are generally too high, especially for moister atmospheres (Freitas *et al.*, 2013).

(5) For the emissivity, a range of possible values are attributed to each of the cases above: values of $\epsilon_{10.5}$ from 0.93 to 1.0 in steps of 0.01, and then, in the case of a GSW model, it is appropriate to prescribe departures from this value for $\epsilon_{12.3}$: −0.015 to 0.035 in steps of 0.01 (excluding cases where $\epsilon_{12.3} > 1.0$).

Figure 2 shows the statistical and geographical properties of the database gathered following those steps, which total 116 profiles. By combining these profiles with the prescribed viewing geometries and surface/low-level conditions proposed in steps 3 to 5, the total number of cases used in the calibration is 906,192. This number is around sixty times larger than the number of simulations made for the validation dataset, which contains the remaining profiles in the SeeBor database, simulated with a random angle within the ZVA range of the Meteosat disk. Low humidity profiles dominate within the distribution, to ensure a proper coverage of the $\mathrm{TCWV}/\ \mathrm{T_{Skin}}$ phase space and its large dynamic range of $\mathrm{T_{Skin}}$ towards low TCWV values. The way the database is built also leads to a greater frequency of profiles gathered over land, since some of the most extreme conditions are only found there. The presence of some marine profiles is not problematic because algorithms also need to cover cases where the LST retrieval is made over small islands or coastal regions. Validation of LST products over large water bodies is also a common practice (e.g., Wan (2008)).

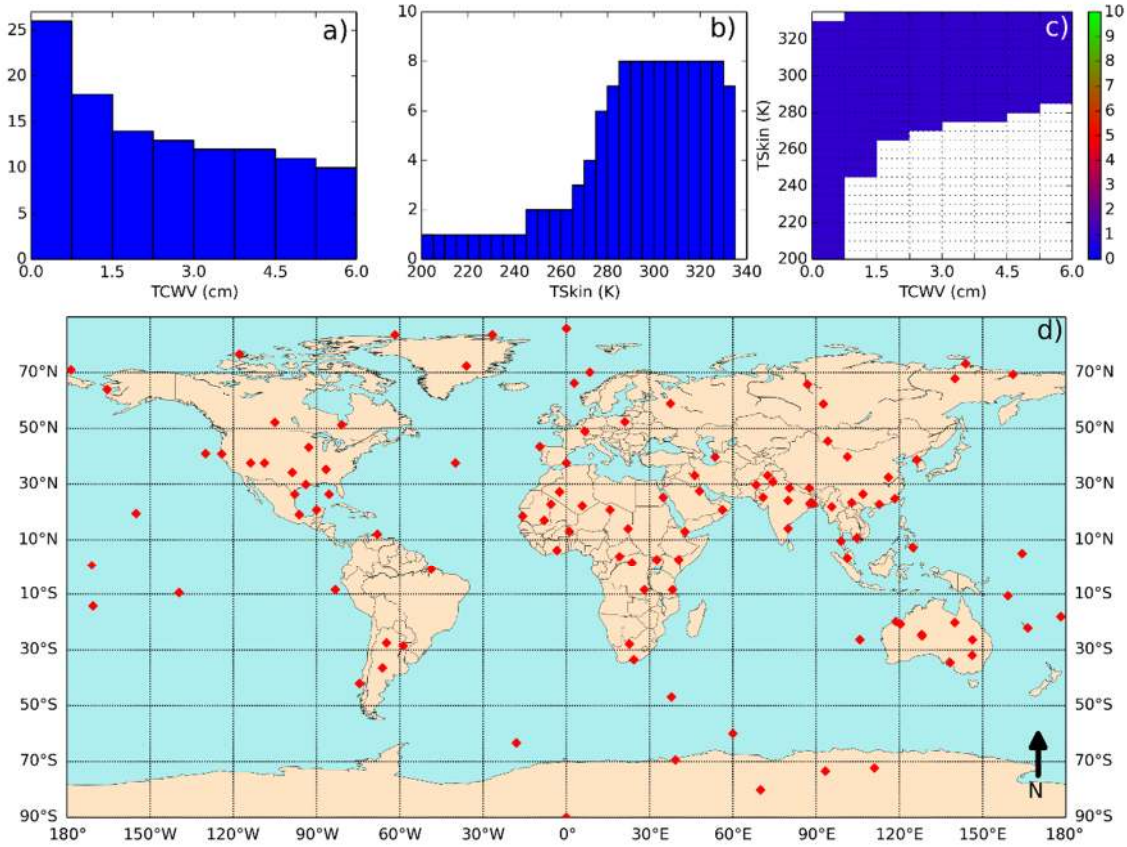

Figure 2 - Main properties of the calibration database: (a) $TCWV$ distribution, (b) T_{Skin} distribution, (c) bivariate $TCWV/T_{Skin}$ distribution, showing one case per bin, and (d) geographical distribution of the selected profiles.

The coefficients, calculated per classes of ZVA and TCWV, using the simulated brightness temperatures of the calibration database are shown in Figure 3. The coefficients vary fairly smoothly throughout the TCWV and ZVA classes, except for cases where very moist atmospheres are observed with high zenith angles. In such conditions the linear combination of the split-window channels cannot reproduce the non-linear path length effects, leading to poor performance of the model in those classes.

A new set of LSTs is calculated using the simulated brightness temperatures of the validation database as input to the GSW model, using the calculated coefficients. The algorithm uncertainty is then estimated by comparing these new LSTs with the "true value" of the skin temperature from the SeeBor database, which in turn served as input to the radiative transfer simulations. The model shows a very small overall bias of around -0.09 K and the RMSE is around 0.94 K (Figure 4a). However, these statistics are not uniform across the whole TCWV/ZVA spectrum (Figure 4b): for ZVAs less than 40° the RMSE is always less than 1.25 K. It grows towards the classes with a combination of high ZVA with high TCWV to values greater than 4 K, in which case the use of the retrieved LSTs is discouraged.

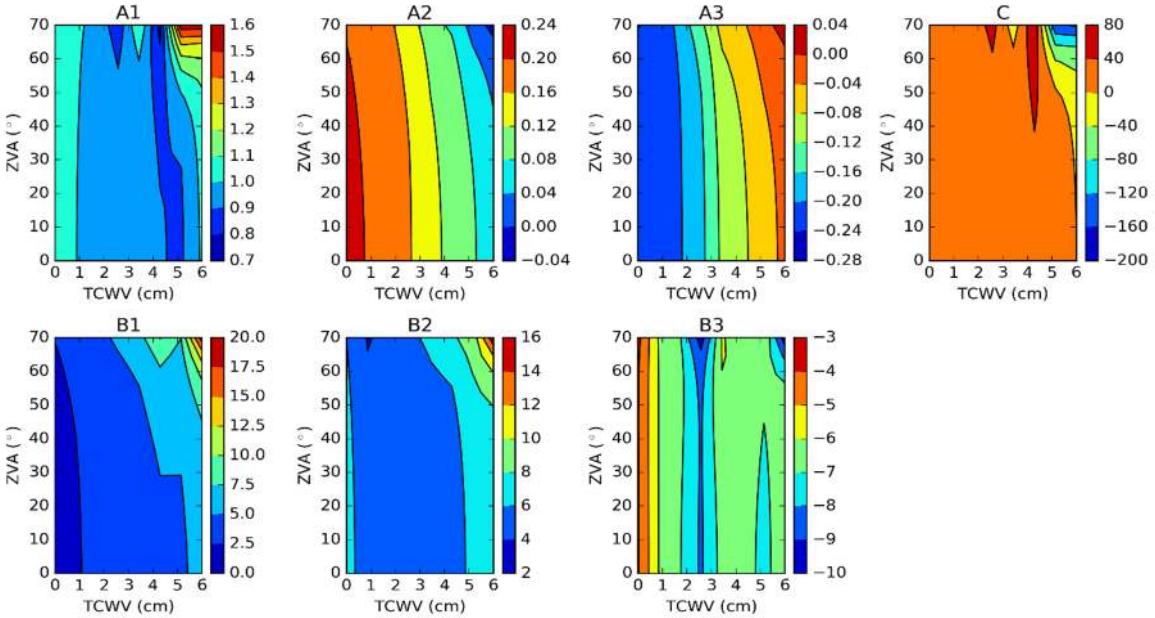

Figure 3 – MTG-FCI GSW model coefficients as function of the TCWV and ZVA.

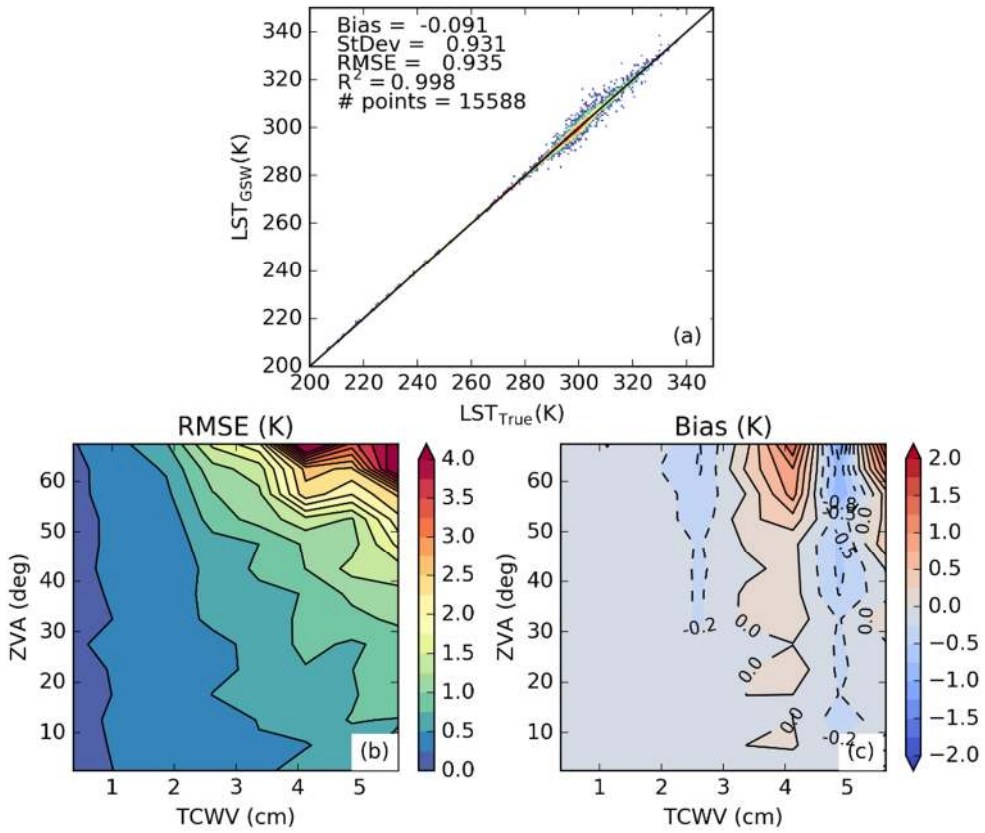

Figure 4 - (a) Comparison of the GSW LST computed with the validation database with the "true value" of the LST used as input of the radiative transfer simulations. Indicated are the bias, standard deviation, RMSE, coefficient of determination and the number of values used. (b) RMSE (K) as a function of TCWV and ZVA. (c) Bias (K) as a function of TCWV and ZVA.

The bias depends somewhat more strongly on TCWV (Figure 4c), resembling the structure of some of the model coefficients (Figure 3). Only in some classes with high ZVA (greater than 50°) and TCWV (greater than 4 cm^{-1}) the bias absolute value exceeds 0.5 K, in which case caution is also recommended when using the retrieved LST.

3.4 Product uncertainty

In a real scenario, we do not have access to the exact GSW inputs $X = (T_{10.5}, T_{12.3}, \epsilon_{10.5}, \epsilon_{12.3})$ and $Y = (W, \Psi)$ (where W denotes the TCWV and Ψ is the ZVA), but only to inaccurate inputs, which we denote by $\hat{X} = \left(\hat{T}_{10.5}, \hat{T}_{12.3}, \hat{\epsilon}_{10.5}, \hat{\epsilon}_{12.3}\right)$ and $\hat{Y} = (\widehat{W}, \widehat{\Psi})$. Therefore, if we still infer the LST according to model (1) replacing the exact GSW inputs with the inaccurate ones, we have a new source of uncertainty on the top of the fitting error ΔLST shown in Figure 4. In the current section, the main uncertainty sources are identified and their impact on the total LST uncertainty estimated.

Potentially, all inputs may introduce errors in retrieved LST values. However, here we only consider the radiometric noise, the uncertainty in surface emissivity and errors in W forecasts. The rectification of the satellite data from the real position to 0° longitude may introduce errors in the determination of the ZVA class. We have opted to ignore the impact of these errors on the overall LST error, taking into account that: (i) the probability of having the wrong class of ZVA for MTG is fairly low, and very unlikely to be missed by more than one class; (ii) the extra GSW error induced by the wrong categorization of ZVA by one class is negligible for low ZVA and only reaches values of 0.5K or higher for very large ZVA (above 60°).

The misclassification of cloudy pixels as clear sky has very high impact on LST products retrieved from IR measurements. According to validation results of the NWC SAF cloud mask for SEVIRI, the expected rate of missed clouds is of the order of 4% (Kerdraon and Le Gléau, 2016). These missed cases often correspond to broken clouds or cases in neighbouring cloudy pixels. We expect statistics for the FCI/MTG cloud mask will not be degraded with respect to that of SEVIRI, and therefore we use those here as a reference. It is very difficult to propagate the uncertainty in cloud identification to LST error bars. Instead, LST retrievals over neighbouring cloudy pixels are flagged.

3.4.1 Framework

Let us define the vector of model coefficients $\theta = (A_1, A_2, A_3, B_1, B_2, B_3, C)$. Notice that the vector θ generated by the fitting process is a function of TCWV and ZVA, i.e., $= \theta(Y)$. Consider the LST estimator $\widehat{LST} = f(\hat{X}, \hat{\theta})$, where $\hat{\theta} = \theta(\hat{Y})$ and $f(X, \theta)$ is the LST estimate given by model (1). A characterization of the model uncertainty is given by:

$$S_{LST} = E\left[\left(f\left(\hat{X}, \hat{\theta}\right) - LST\right)^2 \middle| X, Y\right]^{1/2}, \quad (5)$$

where the operator $E[.|X,Y]$ stands for mean value conditioned to X and Y; i.e. for a given GSW input X,Y, we want to compute the RMSE of the LST estimate. Using the fact that $LST = f(X,\theta) + \Delta LST$ and assuming that $E\left[f\left(\hat{X},\hat{\theta}\right)|X,Y\right] = f(X,\theta)$, we may write:

$$S_{LST}^2 = E\left[\left(f\left(\hat{X},\hat{\theta}\right) - f(X,\theta)\right)^2 \middle| X,Y\right]^{1/2} + \Delta LST^2 \quad (6)$$

By taking a linear approximation of $f\left(\hat{X},\hat{\theta}\right)$ in the neighbourhood of (X,θ) and denoting $\sigma_{X_i}^2 = E\left[\left(\hat{X}_i - X_i\right)^2 | X\right]$ and $\sigma_{\theta_i}^2 = E\left[\left(\hat{\theta}_i - \theta_i\right)^2 | Y\right]$, we are led to:

$$S_{LST}^2 = \sum_i \left(\frac{\partial f}{\partial X_i}\right)^2 \sigma_{X_i}^2 + \sum_j \left(\frac{\partial f}{\partial \theta_j}\right)^2 \sigma_{\theta_i}^2 + \Delta LST^2, \quad (7)$$

where we have assumed that the components of X,Y are mutually independent and that the $E\left[\left(\hat{X}_i - X_i\right)| X\right] = 0$ and $E\left[\left(\hat{\theta}_i - \theta_i\right)| Y\right] = 0$. Next, we study in detail the error due to each individual GSW input.

3.4.2 Impact of sensor noise

The impact of sensor noise on LST is given by the sum of the uncertainties associated to the noise of each split-window channel:

$$S_T^2 = S_{T_{IR1}}^2 + S_{T_{IR2}}^2, \quad (8)$$

where

$$S_{T_{IR1}}^2 = \left(\frac{\partial f}{\partial T_{IR1}}\right)^2 \sigma_{T_{IR1}}^2 \text{ and } S_{T_{IR2}}^2 = \left(\frac{\partial f}{\partial T_{IR2}}\right)^2 \sigma_{T_{IR2}}^2 \quad (9)$$

In this case, the value of $\sqrt{\sigma_{\mathrm{T_{IRn}}}^2}$ is given by the instrument radiometric noise, $NE\Delta T$, to be reported for each channel upon instrument calibration. Values for the FCI channels are yet to be reported.

In the case of the GSW used by the LSA-SAF [eq. (1)], the derivatives with respect to the split-window brightness temperatures are given by:

$$\frac{\partial f}{\partial T_{IR1}} = \frac{1}{2}\left[A_1 + B_1 + (A_2 + B_2)\frac{1-\epsilon}{\epsilon} + (A_3 + B_3)\frac{\Delta\epsilon}{\epsilon^2}\right], \quad (10)$$

$$\frac{\partial f}{\partial T_{IR2}} = \frac{1}{2}\left[A_1 - B_1 + (A_2 - B_2)\frac{1-\epsilon}{\epsilon} + (A_3 - B_3)\frac{\Delta\epsilon}{\epsilon^2}\right] \quad (11)$$

3.4.3 Impact of uncertainties in surface emissivity

The impact of uncertainties in surface emissivity for both split-window channels is given by:

$$S_\epsilon^2 = S_{\epsilon_{IR1}}^2 + S_{\epsilon_{IR2}}^2, \tag{10}$$

where

$$S_{\epsilon_{IR1}}^2 = \left(\frac{\partial f}{\partial \epsilon_{IR1}}\right)^2 \sigma_{\epsilon_{IR1}}^2 \text{ and } S_{\epsilon_{IR2}}^2 = \left(\frac{\partial f}{\partial \epsilon_{IR2}}\right)^2 \sigma_{\epsilon_{IR2}}^2. \tag{11}$$

In the case of the GSW (eq. (1)), the derivatives in eq. (11) are given by:

$$\frac{\partial f}{\partial \epsilon_{IR1}} = \frac{1}{2}\left[-\frac{A_2}{2}\frac{T_{IR1}+T_{IR2}}{\epsilon^2} + A_3\,(T_{IR1}+T_{IR2})\left(\frac{\epsilon-\Delta\epsilon}{\epsilon^3}\right) - B_2\,\frac{T_{IR1}-T_{IR2}}{\epsilon^2} + B_3\,(T_{IR1}-T_{IR2})\left(\frac{\epsilon-\Delta\epsilon}{\epsilon^3}\right)\right], \tag{12}$$

$$\frac{\partial f}{\partial \epsilon_{IR2}} = -\frac{1}{2}\left[\frac{A_2}{2}\frac{T_{IR1}+T_{IR2}}{\epsilon^2} + A_3\,(T_{IR1}+T_{IR2})\left(\frac{\epsilon+\Delta\epsilon}{\epsilon^3}\right) + B_2\,\frac{T_{IR1}-T_{IR2}}{\epsilon^2} + B_3\,(T_{IR1}-T_{IR2})\left(\frac{\epsilon+\Delta\epsilon}{\epsilon^3}\right)\right] \tag{13}$$

Emissivity retrievals are based on the so-called Vegetation Cover Method (VCM; Caselles and Sobrino, 1989; Peres and DaCamara, 2004; Trigo *et al.*, 2008b), where effective channel emissivity for any given pixel is estimated as a weighted average of channel emissivities of dominant bareground and vegetation types within the scene. Furthermore, it is considered that FCI pixels may include a land fraction, F_{Land}, and an in-land water fraction, $(1 - F_{Land})$, and thus the effective pixel emissivity, $\epsilon_{eff_{IRn}}$, is given by:

$$\epsilon_{Land_{IRn}} = \epsilon_{veg_{IRn}} FVC + \epsilon_{bg_{IRn}}(1 - FVC) \tag{14}$$

$$\epsilon_{eff_{IRn}} = \epsilon_{Land_{IRn}} F_{Land} + \epsilon_{Water_{IRn}}, \tag{15}$$

where FVC is the pixel fraction of vegetation cover and $\epsilon_{veg_{IRn}}$, $\epsilon_{bg_{IRn}}$, $\epsilon_{Water_{IRn}}$ are the vegetation, bareground and water emissivities, respectively, for the split-window channel IRn. The values for $\epsilon_{veg_{IRn}}$ and $\epsilon_{bg_{IRn}}$ are available from a Look up Table (LUT),

as they are calculated *a priori* for the land cover classes within the IGBP (Belward, 1996), accounting for the response function of each sensor:

$$\epsilon_{material}(\nu) = \frac{\int_{\nu_{i,1}}^{\nu_{i,2}} \phi_i(\nu)\, \epsilon_{material}(\nu) d\nu}{\int_{\nu_{i,1}}^{\nu_{i,2}} \phi_i(\nu) d\nu} \quad (16)$$

As an example, Table 3 shows the emissivity values estimated for SEVIRI/MSG split-window channels. These values will be recalculated when the FCI response functions are determined more rigorously from sensor calibration.

IGBP Class	FVC ($\Delta FVC = 0.1$)	ϵ_{IR1}	$\Delta\epsilon_{IR1}$	ϵ_{IR2}	$\Delta\epsilon_{IR2}$
Evergreen Forests (needle- and broad-leaf)	0.8	0.99136	0.00560	0.99248	0.00603
Deciduous Forests (needle- and broad-leaf)	0.8	0.98776	0.00515	0.98840	0.00552
Mixed Forest	0.8	0.98952	0.00537	0.99040	0.00577
Closed Shrublands	0.8	0.98918	0.00684	0.99024	0.00617
Open Shrublands	0.5	0.98120	0.00981	0.98355	0.00818
Woody Savannas	0.5	0.97965	0.01105	0.98205	0.00948
Savannas	0.5	0.97945	0.01086	0.98195	0.00936
Grasslands	0.5	0.97930	0.01068	0.98185	0.00904
Permanent Wetlands	0	0.99240	0.00260	0.99160	0.00610
Croplands	0.5	0.98375	0.00606	0.98725	0.00762
Urban & Built-Up	0.1	0.96101	0.00959	0.97320	0.00652
Crop/Natura Veg. Mosaic	0.5	0.98305	0.00592	0.98605	0.00738
Snow & Ice	0	0.98920	0.00650	0.96560	0.02410
Barren Sparsely Vegetated	0.005	0.94802	0.02444	0.96603	0.01831
Water Bodies	0	0.99000	0.00200	0.98560	0.00090

Table 3 – Land Surface Emissivity and respective standard deviation for the MSG-SEVIRI split-window channels, and the corresponding FVC for each IGBP class (Freitas *et al.*, 2010).

Channel emissivity is currently estimated from FVC retrieved by the Land-SAF from SEVIRI/Meteosat (García-Haro *et al.*, 2005), and corresponds to 5-day composites updated on a daily basis. Since FVC is not currently foreseen to be a MTG day-1 product, the MSG-based FVC product will be interpolated to FCI resolution, using the nearest neighbour approach. Thus, FCI emissivity will be estimated applying the VCM to the

SEVIRI FVC daily product, until the FCI-based FVC (to be developed and implemented by the Land-SAF team) is operational.

The uncertainties in retrieved emissivity using the VCM are thoroughly discussed in Trigo *et al.* (2008b). These take into account inaccuracies in the VCM inputs (of the order of 0.1 for FVC; IGBP-class dependent in the case of $\epsilon_{veg_{IRn}}$ and $\epsilon_{bg_{IRn}}$), and errors in the approximation made by equations (14) and (15), which ignore the effect of multiple reflections within the canopies/ground. The same approach is applied to derive emissivity and respective uncertainties for FCI day-1 product (LSA-007). A further source of emissivity errors relies on the classification of each SEVIRI pixel into one of the two categories: "land" with $F_{Land} = 1$; or "water" with $F_{Land} = 0$. To take this into account in the estimation of emissivity uncertainty, we assume an average error of 0.20 in F_{Land}; in coastal pixels, this uncertainty may reach 0.45.

Error bars of channel emissivity, $\Delta\epsilon_{IR1}$ and $\Delta\epsilon_{IR2}$, are to be estimated operationally along with the emissivity values themselves, and later used to estimate LST uncertainty.

3.4.4 Uncertainties in forecasts of atmospheric water vapour content

Since the total column water vapour is used implicitly in the algorithm (i.e. different sets of parameters are used for each class of TCWV values) the uncertainty can not be calculated analytically. The uncertainty due to this parameter is related to the fact that there is a probability of choosing the wrong set of model coefficients because the TCWV forecast may lead to a wrong choice of TCWV class. Therefore, it is estimated a priori as follows: 1) the operational use of the GSW algorithm (1) to retrieve LST from FCI makes use of forecasts of TCWV (*W*) provided by the European Centre for Medium-range Weather Forecasts (ECMWF). To characterize *W* error statistics, we compare ECMWF *W* forecasts (with forecast steps ranging between 12 and 36 h) with the respective analysis, for the 15th of each month for one full year; ECMWF grid points with model cloud cover higher than 10% were excluded. This exercise is repeated regularly (about once per year) to update the uncertainty in ECMWF forecasts. The comparison between *W* forecasts and analysis (the reference value) allows us to estimate the probability $P\left(\widehat{W}_{i_{fc}}|W_{i_{an}}\right)$, i.e., the probability that $\widehat{W}$ belongs to the water vapour content class $W_{i_{fc}}$, given that the true class is $W_{i_{an}}$. 2) The validation database (described in section 3.3) is used to calculate the variance of the LST for each class of ZVA/TCWV. The variance is obtained by simulating each case of the validation database (i_{valid}) with all the possible sets of coefficients corresponding to that ZVA (i_{fc}) and then comparing to the value obtained with the "true" set of coefficients ($LST_{i_{valid}}$). The uncertainty final estimate is provided for each ZVA / forecast TCWV class by multiplying the obtained variance by the probability of a given forecast class does not correspond to the "true" class:

$$S_W^2 = \frac{1}{n_{TCWV}} \sum_{i}^{n_{TCWV}} \sigma^2_{\widehat{W}_{ian}|W_{fc}} P(W_{i_{an}}|\widehat{W}_{fc}), \quad (17)$$

where $\sigma^2_{\widehat{W}_{ian}|W_{fc}}$ is the variance of the errors of LST for a given *W* estimate (i.e., for a given TCWV forecast $\widehat{W}_{fc}$), when the correct value is $W_{i_{an}}$; $P(W_{i_{an}}|\widehat{W}_{fc})$ is the probability that the correct class of TCWV is determined by $W_{i_{an}}$, conditioned by the forecast value of $\widehat{W}_{fc}$; n_{TCWV} is the number of TCWV classes considered.

3.4.5 Total uncertainty of LST retrievals

The estimation of LST error bars, S_{LST}, assumes that all sources of errors described in the previous sections are independent:

$$S_{LST} = \sqrt{S_T^2 + S_\epsilon^2 + S_W^2 + \Delta LST^2} \quad (20)$$

3.4.6 An assessment of LST expected uncertainty

The formulation described above is to be applied when the actual processing chain is in place and actual data is used to calculate the uncertainty on a pixel-by-pixel basis. However, the order of magnitude of each source of uncertainty may be assessed by prescribing "perturbed" inputs within the expected ranges of variability for each input and compare those retrievals with the ones with "unperturbed" values.

The uncertainty due to sensor noise is estimated here assuming values of $NE\Delta T = 0.1$ K for both split-window channels. These were the values reported for the Advanced Himawari Imager (AHI; Bessho *et al.*, 2016), which serves as testbed for the FCI due to their similar characteristics and capabilities. For each case of the validation database, the brightness temperatures were perturbed a sufficiently large number of times to ensure consistency between realizations (we considered 200 times to be enough for this purpose) using a normal distribution with standard deviation of 0.1 K. The comparison of the LST values retrieved from perturbed brightness temperatures versus those from unperturbed ones is illustrated in Figure 5b as a function of the TCWV and ZVA. Uncertainties of less than 0.5 K are found for most of the classes, but grow to around 1 K for classes with both high TCWV and ZVA, i.e., for large optical paths.

Figure 5c shows the uncertainty on LST retrievals exclusively attributed to forecast errors, considering the ECMWF model performance of 2015. These are generally very low (e.g. lower than the sensor noise uncertainty), although they show an increase with the atmospheric moisture content. This is due to the fact that GSW coefficients vary slowly with TCWV for dry-to-moderately dry atmospheres; only for the top right region of the diagram the coefficient values change more rapidly (see Figure

3). Also, the probabilities of ECMWF forecast leading to wrong classes differing by more than one adjacent class are very low, especially for drier atmospheres.

The uncertainty due to the emissivity is estimated using a "bulk" approach, in which the whole spectrum of surface types was grouped into 3 categories: "mostly barren", "sparsely to moderately vegetated" and "vegetated, moist surfaces or inland water bodies". Each class corresponds to an emissivity range, and lower values translate to higher uncertainty. Values in Table 4 were determined by comparison of different global emissivity databases (Seemann *et al.*, 2008; Trigo *et al.*, 2008b). A similar approach to the study of the sensor noise uncertainty was adopted: each case in the validation database was perturbed a sufficiently large number of tries (again 200 times), this time with a flat distribution of emissivity perturbations for each channel with its half-width determined by the values in Table 4. The comparison of the perturbed LSTs versus the unperturbed ones is illustrated in Figure 5 as a function of the TCWV and ZVA, for each of the surface types (panels d, e and f). This source of uncertainty mostly depends on the considered surface type – surfaces with lower emissivities lead to higher uncertainties – and on TCWV – drier atmospheres increase the uncertainty due to emissivity, since under moist conditions the impact of emissivity on the surface emitted radiance is partially compensated by an opposite effect on the (higher) atmospheric radiation reflected by the surface (Trigo *et al.*, 2008b). Moreover, the higher values of $\sigma^2_{\epsilon_{IR10.5}}$ and $\sigma^2_{\epsilon_{IR12.3}}$ are often found in (semi-)arid regions (see Barren Sparsely Vegetated, Savanna, or Woody Savanna land cover types in Table 3), leading to LST inaccuracies of around 1.5 K or more under dry conditions (TCWV below 1.5 cm). In contrast the impact on LST is always below 0.8 K for the moister atmospheres (W > 4.5 cm).

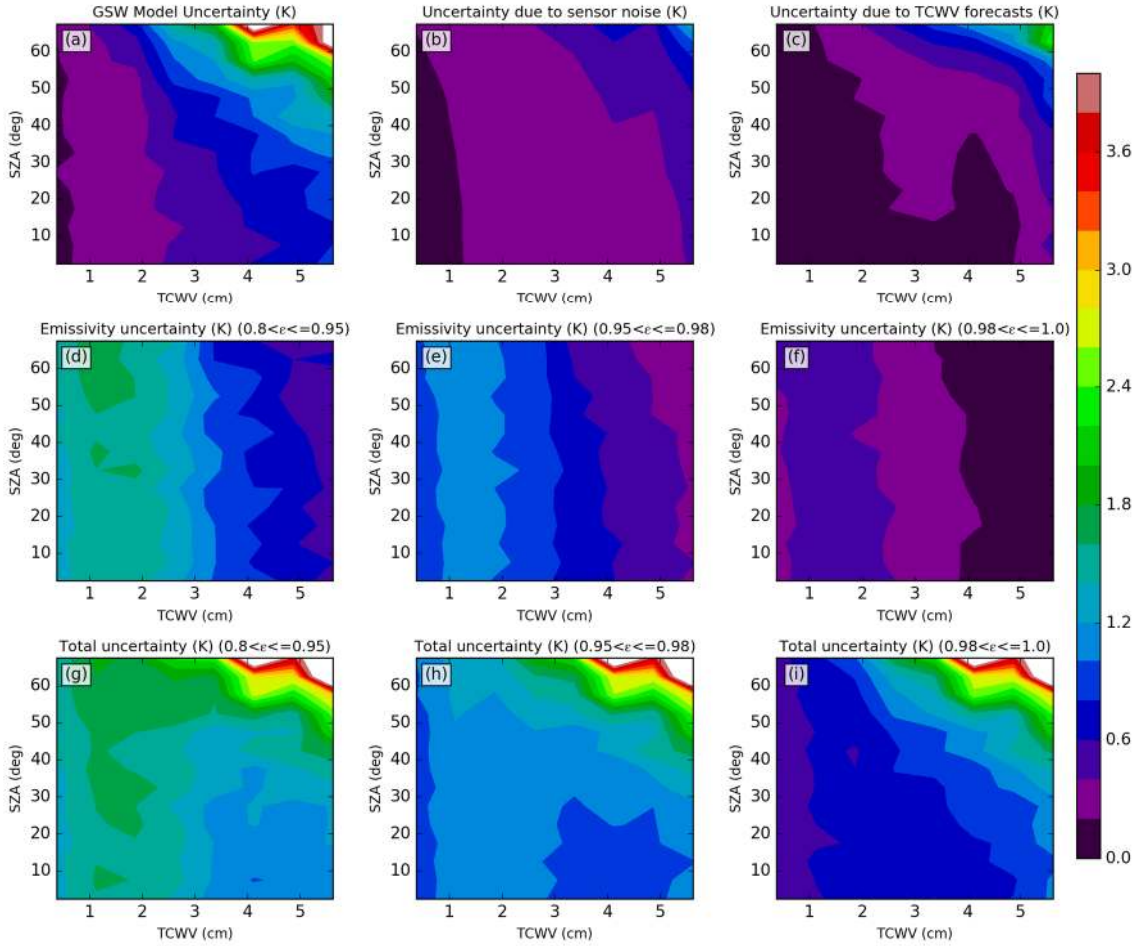

Figure 5 - Uncertainty in LST estimates, measured as the RMSD (°C) between retrieved LST and the validation database true value, considering: (a) the input data are error-free; (b) the sensor noise; (c) the uncertainty associated to total column water vapour forecasts; (d) uncertainty in surface emissivity, for cases where it lies between 0.8 and 0.95 (mostly barren surfaces); (e) uncertainty in surface emissivity, for cases where it lies between 0.95 and 0.98 (sparsely to moderately vegetated surfaces); (f) uncertainty in surface emissivity, for cases where it is higher than 0.95 (vegetated and/or moist surfaces or inland water bodies). The lower row represents total uncertainty, for the emissivity types described above. The results are presented for combinations of W (x-axis) and view zenith angle (y-axis), for the FCI algorithm.

The bottom row of Figure 5 (panels g, h and i) shows the expected total uncertainty of LST for the different scenarios of surface emissivity (and respective uncertainties) obtained with equation (18). Dry atmospheres present the widest range of S_{LST}. such as discussed above, the combination of high uncertainty due to emissivity and low TCWV leads to the high values of total uncertainty, of around 1.5 K for all ZVAs. For moister atmospheres the algorithm uncertainty becomes dominant. For the case of high emissivity surfaces, S_{LST} increases with total water vapour content and view angle, i.e., LST error bars increase for higher optical depths.

The MTLST product, like all LST products derived via a GSW, will be affected by large-scale systematic uncertainties. However, it should be stressed that the most likely

source of systematic uncertainties in the LSA SAF LST products arises from systematic errors in surface emissivity. These will be determined by the reliability of the land-cover classification, the quality of the spectral library and of their conversion into emissivity of natural surfaces. Given its low variability in time, errors in the bareground or vegetation emissivity attributed to any given pixel translates into a source of systematic errors, particularly relevant in arid and sparsely vegetated regions.

Surface type	Emissivity Ranges	$\sigma^2_{\epsilon_{IR10.5}}$	$\sigma^2_{\epsilon_{IR12.3}}$
Mostly barren	$\varepsilon < 0.95$	0.030	0.025
Sparsely to moderately vegetated	$0.95 \leq \varepsilon < 0.98$	0.020	0.010
Vegetated, moist surfaces or inland water bodies	$\varepsilon \geq 0.98$	0.006	0.006

Table 4 - Uncertainty values considered for surface emissivity of FCI channels IR 10.5 and IR 12.3

4 Processing chain

4.1 Algorithm overview

The algorithm flowchart is represented in Figure 6. The main inputs for the LST algorithm are:

- the level 1c Radiances for the split-window channels, centred at 10.5 µm and 12.3 µm; these will be converted to brightness temperatures;
- the cloud mask, which is processed using the corresponding software package to be provided by the NWC-SAF
- satellite zenith viewing angle;
- total column water vapour forecasts, to be provided operationally by the ECMWF
- surface emissivity for the split-window channels.

The surface emissivity is computed by a companion algorithm which uses information from snow cover, a land/sea mask, the Fraction of Vegetation Cover (FVC) also produced at LSA-SAF and a LUT which contains information on the emissivity of different materials and vegetation types. This information is used to characterize the bare ground and vegetation emissivities, since the final emissivity value is an average of both, weighted by the FVC, as described in section 3.4.3).

4.2 Practical Implementation

The estimation of the LST using equation (1) has been implemented by the LSA-SAF both for SEVIRI in the context of the operational production and also in a number of

other projects using other geostationary and polar orbiting sensors such as the imagers on MTSAT and its successor Himawari, the AVHRR on Metop and AATSR on-board Envisat. The transition from the MTSAT to the Himawari was an ideal testbed to prepare for the transition from SEVIRI to the upcoming FCI on MTG, as its day-1 production took place without any major issues.

The biggest challenges are the increase in both spatial and temporal resolution. The number of available channels will increase but consistency between existing channels of SEVIRI and the new ones on FCI is roughly assured. In the case of the LST algorithm the fact that the response functions (which are still preliminary at this stage) are somewhat different for both instruments (see Figure 1) did not seem to introduce a large discrepancy in the LST quality, and the expected uncertainty (Figure 5) is largely similar to what we have for SEVIRI.

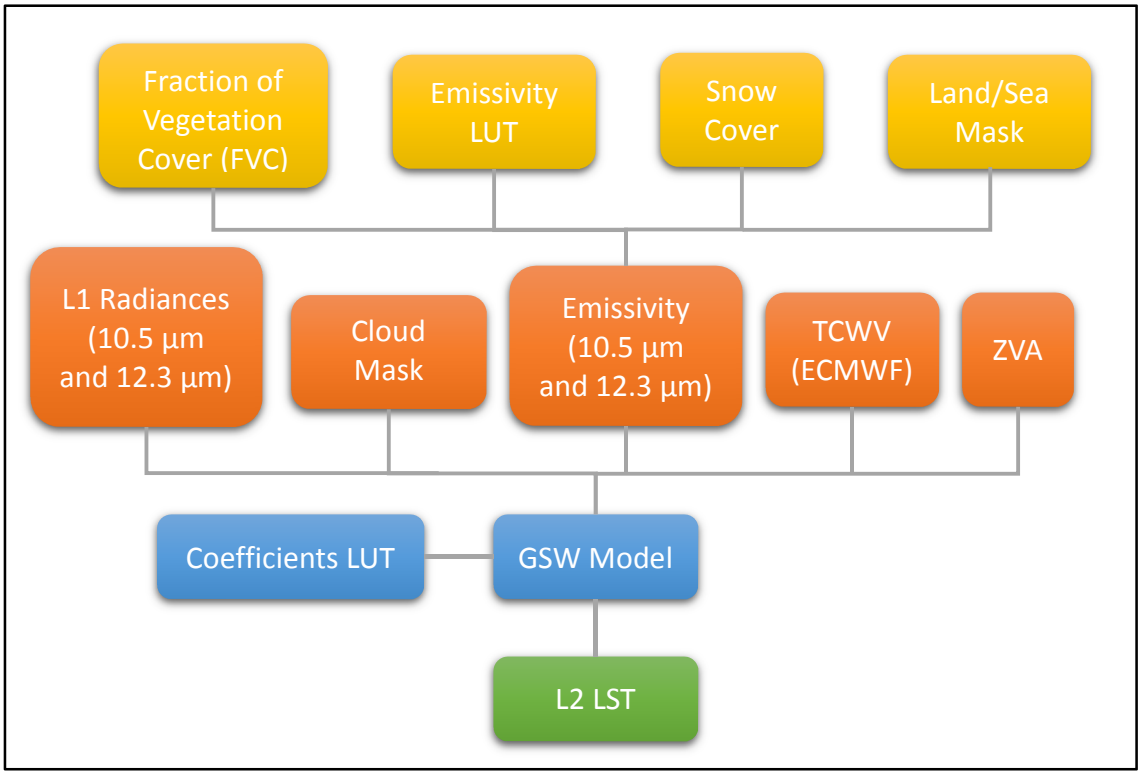

Figure 6 – LST algorithm flowchart

The implementation day-1 LST product for FCI/MTG will take into account the following points:

1) Since LST is only provided over clear-sky pixels, the cloud-mask algorithm is crucial for the quality of the LST final product. In the case of the day-1, the Land-SAF team will use the first release (day-1) of the NWC SAF the cloud mask.

2) The surface emissivity fields, which depend on FVC estimations, will also be derived from the Land-SAF SEVIRI-based FVC, until the corresponding FCI/MTG product (also Land-SAF) is available. As such, a pre-processing to interpolate SEVIRI-FVC to the FCI geostationary 2km grid shall be implemented in the operational chain.

3) The TCWV is provided operationally by the ECWMF and the pre-processing will to interpolate those fields to the FCI geostationary 2km grid will also be implemented, following the similar procedure in place for the SEVIRI processing chain.

4.3 Exception Handling

The following input data per pixel are mandatory to estimate MTLST; if any is missing, MTLST is set to "missing value":

- Brightness temperature for both split-window channels, $T_{10.5}$ and $T_{12.3}$;
- Cloud-mask derived by the NWC-SAF algorithm.

The following input data per pixel are essential to estimate MTLST, but in case of data unavailability, climatological monthly datasets may be used, with a degradation in the quality of the operational retrieval:

- Quality controlled emissivity for both split-window channels, $\epsilon_{10.5}$ and $\epsilon_{12.3}$. These in turn depend on the pixel fraction of vegetation cover, FVC, the pixel land-cover (from the IGBP database), the land-water mask and the snow mask (provided by the H-SAF). A set of monthly climatological fields for both $\epsilon_{10.5}$ and $\epsilon_{12.3}$ will be prepared, to be used in the unlikely event of the daily fields are not processed; as in the case of the SEVIRI processing chain, the monthly emissivity values are based on monthly statistics of FVC.
- Total Column Water Vapour, TCWV, obtained from ECMWF operational forecasts, interpolated to SEVIRI/MSG pixels within the LSA SAF processing chain, as part of the pre-processing package used by all LSA SAF products. If available, the corresponding forecast step from a previous forecast may be used in case of unavailability of the more recent forecast. In the unlikely event TCWV forecasts are not available, the class of the model coefficients is determined using monthly climatologies of the field.

5 References

Bateni, SM, D Entekhabi, D-S Jeng. 2013. Variational assimilation of land surface temperature and the estimation of surface energy balance components. *J. Hydrol*. **481**: 143-156. DOI: 10.1016/j.jhydrol.2012.12.039.

Belward AS. 1996. *The IGBP-DIS global 1km land cover data set (DISCover) – proposal and implementation plans*. Toulouse, France.

Berk A, Anderson GP, Bernstein LS, Acharya PK, Dothe H, Matthew MW, Adler-Golden SM, Chetwynd Jr. JH, Richtsmeier SC, Pukall B, Allred CL, Jeong LS, Hoke ML. 1999. MODTRAN4 radiative transfer modeling for atmospheric correction. *Proc. SPIE*, 348–353. DOI: 10.1117/12.366388.

Bessho K, Date K, Masahiro H, Ikeda A, Imai T, INOUE H, Kumagai Y, Miyakawa T, Murata H, Ohno T, Okuyama A, Oyama R, Sasaki Y, Shimazu Y, Shimoji K, Sumida Y, Suzuki M, Taniguchi H, Tsuchiyama H, Uesawa D, Yokota H, Yoshida R. 2016. An Introduction to Himawari-8/9; Japan's New-Generation Geostationary Meteorological Satellites. *Journal of the Meteorological Society of Japan. Ser. II* **94**(2): 151–183. DOI: 10.2151/jmsj.2016-009.

Borbas EE, Seemann SW, Huang HL, Li J, Menzel WP. 2005. Global profile training database for satellite regression retrievals with estimates of skin temperature and emissivity. *International TOVS Study Conference-XIV Proceedings*.

Bosilovich MG, Radakovich JD, da Silva A, Todling R, Verter F. 2007. Skin Temperature Analysis and Bias Correction in a Coupled Land-Atmosphere Data Assimilation System. *Journal of the Meteorological Society of Japan. Ser. II* **85A**: 205–228. DOI: 10.2151/jmsj.85A.205.

Brutsaert W. 2008. *Hydrology: An Introduction. 3rd ed*. *Hydrology: An Introduction*. DOI: 10.2277/0521824796.

Bulgin CE, Embury O, Merchant CJ. 2016. Sampling uncertainty in gridded sea surface temperature products and Advanced Very High Resolution Radiometer (AVHRR) Global Area Coverage (GAC) data. *Remote Sensing of Environment* **177**: 287–294. DOI: 10.1016/j.rse.2016.02.021.

Caparrini F, Castelli F, Entekhabi D. 2004. Variational estimation of soil and vegetation turbulent transfer and heat flux parameters from sequences of multisensor imagery. *Water Resources Research* **40**(12): 1–15. DOI: 10.1029/2004WR003358.

Caselles V, Sobrino JA. 1989. Determination of frosts in orange groves from NOAA-9 AVHRR data. *Remote Sensing of Environment* **29**(2): 135–146. DOI: http://dx.doi.org/10.1016/0034-4257(89)90022-9.

Coll C, Caselles V, Galve JM, Valor E, Niclòs R, Sánchez JM. 2006. Evaluation of split-window and dual-angle correction methods for land surface temperature retrieval from Envisat/Advanced Along Track Scanning Radiometer (AATSR) data. *Journal of Geophysical Research Atmospheres* **111**(12). DOI: 10.1029/2005JD006830.

Crago RD, Qualls RJ. 2014. Use of land surface temperature to estimate surface energy fluxes: Contributions of Wilfried Brutsaert and collaborators. *Water Resources Research* **50**(4): 3396–3408. DOI: 10.1002/2013WR015223.

Dash P, Göttsche F-M, Olesen F-S, Fischer H. 2001. Retrieval of land surface temperature and emissivity from satellite data: Physics, theoretical limitations and current methods. *Journal of the Indian Society of Remote Sensing* **29**(I): 23–30. DOI: 10.1007/BF02989910.

Duguay-Tetzlaff A, Bento VA, Göttsche FM, Stöckli R, Martins JPA, Trigo I, Olesen F, Bojanowski JS., daCamara, Kunz HK. 2015. Meteosat Land Surface Temperature Climate Data Record:Achievable Accuracy and Potential Uncertainties. *Remote Sens*. **7**, 13139-13156. DOI: 10.3390/rs71013139

Freitas SC, Trigo IF, Bioucas-dias JM, Göttsche F. 2010. Quantifying the Uncertainty of Land Surface Temperature Retrievals From SEVIRI / Meteosat. **48**(1): 523–534.

Freitas SC, Trigo IF, Macedo J, Barroso C, Silva R, Perdigão R. 2013. Land surface temperature from multiple geostationary satellites. *International Journal of Remote Sensing* **34**(9–10): 3051–3068. DOI: 10.1080/01431161.2012.716925.

Gao C, Tang B-H, Wu H, Jiang X, Li Z-L. 2013. A generalized split-window algorithm for land surface temperature estimation from MSG-2/SEVIRI data. *International Journal of Remote Sensing* **34**(12): 4182–4199. DOI: 10.1080/01431161.2013.773408.

García-Haro FJ, Sommer S, Kemper T. 2005. A new tool for variable multiple endmember spectral mixture analysis (VMESMA). *International Journal of Remote Sensing* **26**(September 2014): 2135–2162. DOI: 10.1080/01431160512331337817.

Ghent, D, Kaduk J, Remedios J, Ardö J, Balzter H. 2010. Assimilation of land surface temperature into the land surface model JULES with an ensemble Kalman filter. *J. Geophys Res*. **115**, D19112. DOI: 10.1029/2010JD014392

Hulley GC, Hook SJ, Abbott E, Malakar N, Islam T, Abrams M. 2015. The ASTER Global Emissivity Dataset (ASTER GED): Mapping Earth's emissivity at 100 meter spatial scale. *Geophysical Research Letters* **42**(19): 7966–7976. DOI: 10.1002/2015GL065564.

Jiang GM, Li ZL. 2008. Split-window algorithm for land surface temperature estimation from MSG1-SEVIRI data. *International Journal of Remote Sensing* **29**(20): 6067–6074. DOI: 10.1080/01431160802235860.

Jiménez-Muñoz JC, Sobrino J a. 2006. Error sources on the land surface temperature retrieved from thermal infrared single channel remote sensing data. *International Journal of Remote Sensing* **27**(737628706): 999–1014. DOI: 10.1080/01431160500075907.

Jin M. 2004. Analysis of Land Skin Temperature Using AVHRR Observations. *Bulletin of the American Meteorological Society* **85**(4): 587–600. DOI: 10.1175/BAMS-85-4-587.

Jin M, Dickinson RE, Zhang DL. 2005. The footprint of urban areas on global climate as characterized by MODIS. *Journal of Climate* **18**(10): 1551–1565. DOI: 10.1175/JCLI3334.1.

Kerdraon G, Le Gléau H. 2016. *Scientific and Validation report for the Cloud Product Processors of the NWC/GEO.NWC/CDOP2/GEO/MFL/SCI/VR/Cloud, Issue 1, Rev. 0*. .

Kustas WP, Norman JM. 1996. Use of remote sensing for evapotranspiration monitoring over land surfaces. *Hydrological Sciences Journal-Journal Des Sciences*

Hydrologiques **41**(4): 495–516. DOI: 10.1080/02626669609491522.

Li Z-L, Tang B-H, Wu H, Ren H, Yan G, Wan Z, Trigo IF, Sobrino J a. 2013. Satellite-derived land surface temperature: Current status and perspectives. *Remote Sensing of Environment* **131**: 14–37. DOI: 10.1016/j.rse.2012.12.008.

Martins JP, Trigo I, Bento V, da Camara C. 2016. A Physically Constrained Calibration Database for Land Surface Temperature Using Infrared Retrieval Algorithms. *Remote Sensing*, 808. DOI: 10.3390/rs8100808.

Mattar C, Durán-Alarcón C, Jiménez-Muñoz JC, Santamaría-Artigas A, Olivera-Guerra L, Sobrino JA. 2015. Global Atmospheric Profiles from Reanalysis Information (GAPRI): a new database for earth surface temperature retrieval. *International Journal of Remote Sensing*. Taylor & Francis **36**(19–20): 5045–5060.

Mitchell KE, Lohmann D, Houser PR, Wood EF, Schaake JC, Robock A, Cosgrove B a, Sheffield J, Duan Q, Luo L, Higgins RW, Pinker RT, Tarpley JD, Lettenmaier DP, Marshall CH, Entin JK, Pan M, Shi W, Koren V, Meng J, Ramsay BH, Bailey A a. 2004. The multi-institution North American Land Data Assimilation System (NLDAS): Utilizing multiple GCIP products and partners in a continental distributed hydrological modeling system. *J. Geophys. Res.* **109**(D7): D07S90--. DOI: 10.1029/2003JD003823.

Peres LF, DaCamara CC. 2004. Land surface temperature and emissivity estimation based on the two-temperature method: sensitivity analysis using simulated MSG/SEVIRI data. *Remote Sensing of Environment* **91**(3–4): 377–389. DOI: 10.1016/j.rse.2004.03.011.

Prata AJ. 1993. Land surface temperatures derived from the advanced very high resolution radiometer and the along-track scanning radiometer: 1. Theory. *Journal of Geophysical Research* **98**(D9): 16689–16702. DOI: 10.1029/93JD01206.

Prata F. 2002. *Land Surface Temperature Measurement from Space : AATSR Algorithm Theoretical Basis Document*. Aspendale, Australia.

Qin J, Liang S, Member S, Liu R, Zhang H, Hu B, Land AS, Model S. 2007. A Weak-Constraint-Based Data Assimilation Scheme for Estimating Surface Turbulent Fluxes. **4**(4): 649–653.

Schmetz J, Pili P, Tjemkes S, Just D, Kerkmann J, Rota S, Ratier A. 2002. An introduction to Meteosat Second Generation (MSG). *Bulletin of the American Meteorological Society* **83**(7): 977–992. DOI: 10.1175/BAMS-83-7-Schmetz-2.

Seemann SW, Borbas EE, Knuteson RO, Stephenson GR, Huang HL. 2008. Development of a global infrared land surface emissivity database for application to clear sky sounding retrievals from multispectral satellite radiance measurements. *Journal of Applied Meteorology and Climatology* **47**: 108–123. DOI: 10.1175/2007JAMC1590.1.

Sobrino JA, Romaguera M. 2004. Land surface temperature retrieval from MSG1-SEVIRI data. *Remote Sensing of Environment* **92**(2): 247–254. DOI: 10.1016/j.rse.2004.06.009.

Sun D, Pinker RT. 2003. Estimation of land surface temperature from a Geostationary Operational Environmental Satellite (GOES-8). *Journal of Geophysical Research* **108**(D11): 4326. DOI: 10.1029/2002JD002422.

Trigo IF, Boussetta S, Viterbo P, Balsamo G, Beljaars A, Sandu I. 2015. Comparison of model land skin temperature with remotely sensed estimates and assessment of surface-atmosphere coupling. *Journal of Geophysical Research: Atmospheres* **120**(23): 12096–12111. DOI: 10.1002/2015JD023812.

Trigo IF, Monteiro IT, Olesen F, Kabsch E. 2008a. An assessment of remotely sensed land surface temperature. *Journal of Geophysical Research* **113**(D17): 1–12. DOI: 10.1029/2008JD010035.

Trigo IF, Peres LF, DaCamara CC, Freitas SC. 2008b. Thermal Land Surface Emissivity Retrieved From SEVIRI/Meteosat. *IEEE Transactions on Geoscience and Remote Sensing* **46**(2): 307–315. DOI: 10.1109/TGRS.2007.905197.

Trigo IF, Viterbo P. 2003. Clear-Sky Window Channel Radiances: A Comparison between Observations and the ECMWF Model. *Journal of Applied Meteorology* **42**(10): 1463–1479. DOI: 10.1175/1520-0450(2003)042<1463:CWCRAC>2.0.CO;2.

Wan Z. 2008. New refinements and validation of the MODIS Land-Surface Temperature/Emissivity products. *Remote Sensing of Environment* **112**(1): 59–74. DOI: http://dx.doi.org/10.1016/j.rse.2006.06.026.

Wan Z, Dozier J. 1996. A Generalized Split- Window Algorithm for Retrieving Land-Surface Temperature from Space. *IEEE Transactions on Geoscience and Remote Sensing* **34**(4): 892–905.

Wan Z, Wang P, Li X. 2004. Using MODIS Land Surface Temperature and Normalized Difference Vegetation Index products for monitoring drought in the southern Great Plains, USA. *International Journal of Remote Sensing* **25**(February 2015): 61–72. DOI: 10.1080/0143116031000115328.

Yu Y, Privette JL, Pinheiro AC. 2008. Evaluation of Split-Window Land Surface Temperature Algorithms for Generating Climate Data Records. *IEEE Transactions on Geoscience and Remote Sensing* **46**(1): 179–192. DOI: 10.1109/TGRS.2007.909097.

Annex – Acronym List

AHI	Advanced Himawari Imager
AVHRR	Advanced Very High Resolution Radiometer
ECMWF	European Centre for Medium-range Weather Forecasts
EUMETSAT	European Organization for the Exploitation of Meteorological Satellites
FCI	Flexible Combined Imager
FDS	Full Disk Scan
FVC	Fraction of Vegetation Cover
Himawari	JMA geostationary satellite
IR	Infra-red
IRS	Infra-red sounder
JMA	Japan Meteorological Agency
Land-SAF	(or LSA SAF) SAF on Land Surface Analysis
LI	Lightning Imager
LST	Land Surface Temperature
Metop	EUMETSAT Porlar Satellites
MSG	Meteosat Second Generation
MTG	Meteosat Third Generation
MTG-I	MTG Imaging satellites
MTG-S	MTG Sounding satellites
NIR	Near-Infrared
NWC SAF	SAF on Support to Nowcasting and Very Short Range Forecasting
NWP	Numerical Weather Prediction
NWP SAF	SAF on Numerical Weather Prediction
RRS	Regional-Rapid-Scan
SAF	Satellite Applications Facility
SEVIRI	Spinning Enhanced Visible and Infrared Imager
Tair	near surface Air Temperature
TCWV	Total Column Water Vapour
Tskin	Skin or Surface Temperature
UVN	Ultraviolet Visible Near-infrared
VCM	Vegetation Cover Method
VIS	Visible
ZVA	Zenith Viewing Angle